NANO · MICRO small
www.small-journal.com

Investigating the Role of Surface Roughness and Defects on EC Breakdown, as a Precursor to SEI Formation in Hard Carbon Sodium-Ion Battery Anodes

Emilia Olsson, Jonathon Cottom, Hande Alptekin, Heather Au, Maria Crespo-Ribadeneyra, Maria-Magdalena Titirici, and Qiong Cai**

Hard carbon (HC) anodes together with ethylene carbonate (EC)-based electrolytes have shown significant promise for high-performing sodium-ion batteries. However, questions remain in relation to the initial contact between the carbon surface and the EC molecules. The surface of the HC anode is complex and can contain both flat pristine carbon surfaces, curvature, nanoscale roughness, and heteroatom defects. Combining density functional theory and experiments, the effect of different carbon surface motifs and defects on EC adsorption are probed, concluding that EC itself does not block any sodium storage sites. Nevertheless, the EC breakdown products do show strong adsorption on the same carbon surface motifs, indicating that the carbon surface defect sites can become occupied by the EC breakdown products, leading to competition between the sodium and EC fragments. Furthermore, it is shown that the EC fragments can react with a carbon vacancy or oxygen defect to give rise to CO_2 formation and further oxygen functionalization of the carbon surface. Experimental characterization of two HC materials with different microstructure and defect concentrations further confirms that a significant concentration of oxygen-containing defects and disorder leads to a thicker solid electrolyte interphase, highlighting the significant effect of atomic-scale carbon structure on EC interaction.

1. Introduction

The need for society to transition to a green and sustainable energy economy is pressing with a clear imperative to decarbonize many sectors including electricity generation, transport, and industry. Next-generation battery technologies are receiving increasing attention, with the promise of decarbonizing transportation systems by providing power sources for electric vehicles, as well as decarbonizing electricity generation by providing integrated grid storage for renewable energy sources such as wind and solar.[1,2] Lithium (Li)-ion batteries (LIBs), which offer high energy and power energy densities with a reasonably long lifetime, are the ideal battery technologies for electric vehicles and mobile devices. For integrated grid-based storage, sodium (Na)-ion batteries (NIBs) have emerged as a promising alternative and complement to LIBs, thanks to the abundance, wide availability, and low cost of Na-based compounds.[3–6]

E. Olsson, Q. Cai
Department of Chemical and Process Engineering
University of Surrey
Guildford GU2 7XH, UK
E-mail: e.olsson@arcnl.nl; q.cai@surrey.ac.uk

E. Olsson, H. Alptekin, H. Au, M. Crespo-Ribadeneyra, M.-M. Titirici
Department of Chemical Engineering
Imperial College London
London SW7 2AZ, UK

E. Olsson
Advanced Research Center for Nanolithography
Science Park 106, Amsterdam 1098 XG, The Netherlands

The ORCID identification number(s) for the author(s) of this article can be found under https://doi.org/10.1002/smll.202200177.

DOI: 10.1002/smll.202200177

E. Olsson
Institute of Physics
University of Amsterdam
Science Park 904, Amsterdam 1098 XH, The Netherlands

J. Cottom
Department of Physics and Astronomy
University College London
London WC1E 6BT, UK

J. Cottom
Leiden Institute of Chemistry
University of Leiden
Leiden 2333 CC, The Netherlands

H. Alptekin
Department of Materials
Imperial College London
Exhibition Road, London SW7 2AZ, UK

Unlike conventional LIBs which use graphite for the anode, NIBs have adopted hard carbon (HC) anodes, as Na ions cannot be intercalated into graphite at high concentrations.[7] HC has been widely studied as a suitable anode for NIBs and is a disordered material containing regions of planar graphitic stacks, nanopores, curved motifs, edges (with varying terminations), and basal plane (BP) surfaces.[8–15] These carbons can be synthesized from a variety of precursors, including biomass, opening the possibility for these anode materials to play an important part in the circular economy.[16,17] The atomic scale structure of HC is highly complex and dependent on the precursors employed.[8,10,18–22] Previous studies have shown that carbon structural motifs, defects, and composition play a major role in the reversible (de)sodiation of HCs.[8–12,23,24]

During battery cycling, a solid electrolyte interphase (SEI) layer forms on these HC anodes, the composition of which is dependent on the HC surface structure and the composition of the electrolyte.[25–28] NIB electrolytes usually employ an organic solvent, typically carbonates such as ethylene carbonate (EC), with a thinning agent such as dimethyl carbonate (DMC), or ethyl methyl carbonate (EMC) added to overcome the high viscosity and melting point (36 °C) of EC.[28] These organic solvents react with the anode surface, leading to the formation of a surface film that can affect the device performance (i.e., the starting points of the SEI).[29] The ultimate composition of NIB electrolyte is still under discussion and it is possible that the electrolyte composition will be variable for different NIB chemistries and applications to maximize performance. Most NIBs (and indeed also LIBs) do, however, contain EC, which makes the understanding of the EC-HC interaction at the atomic scale imperative. Previously, we investigated the effect of the electrolyte salt ($NaClO_4$ and $NaPF_6$) on the SEI formation in HC anodes.[6] Here we extend the study to probe the effect of carbon surface structure and defects on EC organic solvent and fragment immobilization. In general, the organic solvent should have a low viscosity, high dielectric constant, good electrochemical stability, thermal stability, and high conductivity of Na-ions.[30,31] It has been shown that a significant concentration of EC in the electrolyte is beneficial to forming a stable SEI.[30,32] Scanning electron microscopy (SEM) images of HC anodes in EC: propylene carbonate (PC) electrolyte showed that there was no significant further decomposition of electrolyte at the electrode surface after cycling even at 75 °C, indicating that the initial contact between the liquid electrolyte and the solid anode is crucial for the cycling behavior and SEI formation.[32,33] Atomic-scale understanding of the anode electrolyte interphase is a key step toward more efficient and longer lifetime NIBs. Previous studies have identified SEI constituents due to EC breakdown, with computational studies exploring the reaction pathways and associated transition state barrier heights for EC dissociation in a vacuum, on graphene and metal surfaces.[34–37] Density functional theory (DFT) and ab initio molecular dynamics (AIMD) studies provide important insights into the initial stages of electrolyte breakdown and the associated SEI formation. To study the interaction of EC with HC surfaces, previous studies have focused on smooth surfaces, graphene (and graphite) basal planes, and graphite edges.[6,8,11,12,23,33,38] It is worth noting that in a realistic battery employing HC as an anode, the EC solvent may also come into contact with heteroatom defects (such as O-containing defects) and curved motifs commonly found in HC. HC surfaces not only consist of atomically smooth basal plane surfaces but also a degree of curvature, herein forthwith referred to as roughness.[8,10,39,40,41] Employing DFT, we can assess the initial interaction between the EC and these HC surface motifs at the atomic scale.

This paper explores the atomic-scale initial HC | EC interphase formation, using an array of HC model systems constructed based upon experimental X-ray photoelectron spectroscopy (XPS) and transmission electron microscopy (TEM) characterization of an HC sample in EC, as well as insights from our previous work.[8,9,11,12,23,24] The HC models consider surface roughness (as defined in Section 2.1), vacancies, and oxygen from the experimental characterization. We include a series of defects: O_C (oxygen substitutional defect), $2O_C$ (double substitutional oxygen defect), V_C (carbon vacancy), and O_CV_C (oxygen substitutional defect with carbon vacancy) at distinct positions in the carbon model. These defects have also been previously identified as playing a significant role in Na storage behavior.[8,10,23,24,42] Herein, we extend to examine the effect of these defects on EC interaction. The interactions of EC with various HC surface morphologies (Section 2.1) and defects (Section 2.2) are then characterized to illustrate the binding and breakdown of EC at the HC surfaces. Finally, AIMD is employed to capture EC breakdown at the disordered surface (Section 2.3). The SEI formation on two HC samples in EC electrolyte is also probed experimentally to validate the computational results in Section 2.5.

2. Results and Discussion

In our previous work, we have employed a range of carbon models to represent different motifs in HC anodes.[11] These include pristine and defective graphene sheets to model the flat surface using a basal plane (BP) model (see Figure S1a, Supporting Information), and sinusoidal and oval reconstructed surfaces to capture the abrupt surface (see Figure S1b, Supporting Information).[11,12,23,24] Transmission electron microscopy (TEM) images of the two hard carbon materials prepared in this work (**Figure 1**), however, suggest that the HC surfaces are not atomically smooth, but that there is a degree of roughness, with a peak to trough distance of 1 nm. Similar observations have also been made previously.[8,39,10,40,41] To approximate this computationally, we have created a rough model containing curved carbon surfaces with a trough of 7.5 Å depth in between the two elevated carbon sheets to represent this roughness (Figure 1, with the full periodic model shown in Figure S1c, Supporting Information). Whilst this is a significant simplification, it allows the lattice, defects, and their interactions with the EC molecule to be considered in isolation. As H-terminated graphitic surfaces have previously been shown to be unstable in EC, these surfaces are not included in the current study (previously calculated in ref. [11,28].

2.1. EC Adsorption

To assess the interaction of the carbon surfaces with the EC electrolyte, we performed DFT simulations to describe the

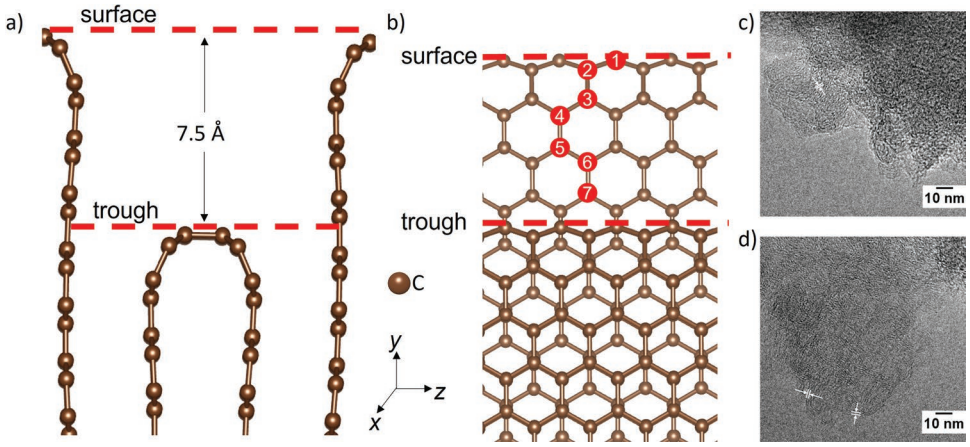

Figure 1. Schematic view of the rough interface indicating a) the 7.5 Å trough in the rough model (showing the *y*–*z* plane of the 3D rough model), and b) the different lattice sites for the defect and adsorption study (showing the *x*–*y* plane of the 3D rough model). Brown spheres are carbon atoms. TEM images of c) ST1000 and d) ST1500 show the rough curved edges in hard carbon samples, with peak–trough distances indicated by the arrows.

EC-surface binding interaction (**Figure 2**). From the adsorption energies (E_{ads}) calculated according to Equation (1) in Section 4, no strong interaction between an EC molecule and the model in Figure 1 could be found. For the rough models, a similar situation is observed. The strongest EC adsorption energy (–0.60 eV) is obtained when the EC carbonyl oxygen sits 2.92 Å from the carbon lattice with the EC molecule aligned toward positions 5–7, that is, the less curved part of the model (Figure 2b). When

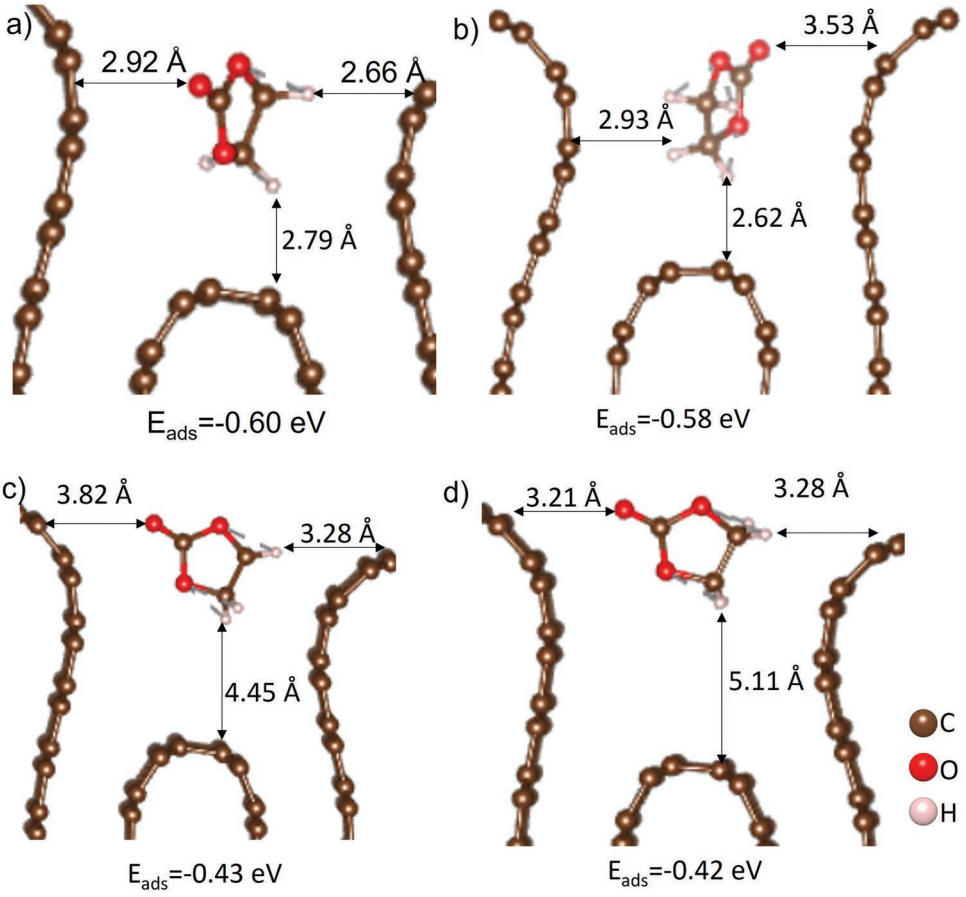

Figure 2. Optimized EC configurations and adsorption energies at intercalation-type (a,b) and surface-type (c,d) sites in the rough model. Brown spheres are carbon, red oxygen, and white hydrogen. Interatomic distances between the EC molecule and the closest carbon lattice points are indicated with double-ended arrows.

the EC molecule sits with the carbonyl oxygen toward one of the carbon planes, and the hydrogen tails toward the other, the adsorption is weaker (Figure 2c,d). This indicates that the configuration of the EC molecule in relation to the carbon lattice influences the EC-carbon interaction. The interaction of EC with a pristine basal plane is very weak, as shown by the low adsorption energy (–0.46 eV, see Supporting Information for more details) obtained when the carbonyl oxygen is closest to the graphene surface. In the case of the rough model (Figure 2), the calculated adsorption energies (between –0.42 and –0.6 eV) suggest slightly stronger interactions between the EC molecules and the carbon planes, yet they remain weak. Such a low level of EC adsorption should not lead to EC immobilization at these sites, nor hinder sodium from entering the HC anode, however, it is suggested that the curvature leads to reduced EC mobility, as compared to EC on the basal plane surface.

To assess the effect of surface roughness on EC mobility, a series of AIMD simulations of the EC-carbon interface was conducted, whilst varying the trough depth (1–7.5 Å) of the rough model (Figure S2, Supporting Information). Interestingly, similar EC diffusion coefficients were obtained for all the rough model systems of different trough depths (6.41×10^{-9} m^2 s^{-1} for roughness 1 Å, 9.49×10^{-9} m^2 s^{-1} for roughness 2 Å, 9.62×10^{-9} m^2 s^{-1} for roughness 5 Å, and 7.72×10^{-9} m^2 s^{-1} for roughness 7.5 Å), suggesting a degree of model independence when the EC adsorption and diffusion is concerned for the roughness. For comparison, AIMD simulations are also performed for EC molecules on the basal plane interface. The same weakly interacting picture was observed although a slight rumpling of the graphene sheets was seen (Figure S3, Supporting Information). The calculations confirmed an EC diffusion coefficient of 1.98×10^{-8} m^2 s^{-1} for the basal plane model, higher than those calculated with the rough model of different roughness (indicated by trough depth values). This agrees with the trend in adsorption energy in Figure 2, with the stronger interaction between EC and the rough models leading to more sluggish EC diffusion than on the basal plane. This observation further confirms that the SEI is expected to be thinner at the basal plane than on edge sites (assuming the higher mobility and lower adsorption energy of EC leads to less trapping and degradation of EC at the basal plane as compared to the rough models), which has previously been observed experimentally in graphite anodes for LIBs.[28] In real HC anodes, significant defect and heteroatom concentrations have been identified. To understand the binding and vectors for breakdown, further consideration of the defect-EC interaction is required.

2.2. EC Adsorption at Defect Sites

In our previous work,[11,23,24] defects have a marked impact on the adsorption characteristics and hence mobility of metal ions in HC. In this work, the effect of the previously considered defects on EC–HC interactions is characterized. A range of defects is considered, including an oxygen substitutional defect (O_C), double substitutional oxygen defect ($2O_C$), carbon vacancy (V_C), and oxygen substitutional defect with carbon vacancy ($O_C V_C$). These defects are placed at different positions in the rough model, according to the seven lattice positions (P1–P7) labeled in Figure 1b. In each case, P1 is at the offset surface and then at each lattice position until the other surface (trough) is reached (P7). **Figure 3** shows the formation energy of each defect at each position.

As shown in Figure 3b, the defect formation energy generally decreases as the surface top is approached, with either the defect at the surface top (P1) or directly below (P2) being the lowest energy configuration. This is in common with our previous results for HC defects at the curved surface models,[23] indicating that the defects would be more likely at the surface top. Some small variations of the defect formation energy are observed with different lattice positions from P1 to P7. This is because the strain increases as the interface (i.e., surface top) is approached, and the interaction between adjacent graphene sheets is also largely absent with the layers being at a maximum separation of 10 Å.[12,24] The same effect was observed for the models with a shallower trough (Figure S4, Supporting

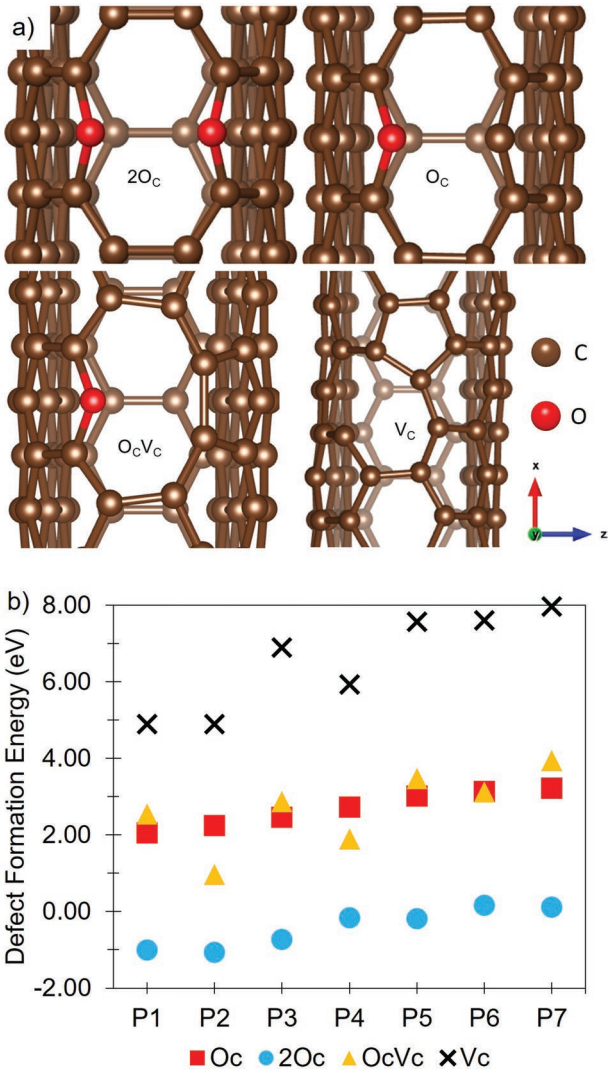

Figure 3. a) Zoomed-in view of the optimized structure of the defects at the P1 position, where brown spheres are carbon atoms, red oxygen, and white hydrogen. b) Defect formation energy of the intrinsic and O-defects as a function of lattice positions in a rough model with a trough depth of 7.5 Å.

Information). The variations observed from the smooth trend for the O_CV_C and V_C defects can be understood by considering the local strain environment as a function of defect position. This local strain reaches a maximum at P4 where a deviation from the ideal planar structure is at a maximum with a single C−C aligned perpendicular to the surface. The introduction of the O_CV_C and V_C defects at this position releases a significant portion of the strain via the relaxation of a 5-membered ring (and a C-dangling bond for the V_C), resulting in two near planar rings.

To understand EC interaction with the defective models, the adsorption energy of an EC molecule in the defective rough models (with each defect at different lattice positions P1–P7) was calculated (as shown in **Figure 4** and Figure S5, Supporting Information), in comparison to the EC adsorption energy on the basal plane (Figure S6, Supporting Information) and the curved surface (Figure S7, Supporting Information) with the same defects. Three distinct adsorption regimes are observed in Figure 4. In P1 and P2, the EC shows surface adsorption interaction with the edge of a single C-sheet (giving similar adsorption energies and configurations seen for the abrupt surface, in Figure S7, Supporting Information). P3–P5 shows an intermediate binding behavior as the EC moves from single sheet surface adsorption toward intercalation-like behavior, where the EC sits between two carbon sheets (just above the trough in Figure 1). Finally, the strongest interaction between the EC molecule and the defect is seen for defect sites P5–P7, which represents the intercalation of the EC molecule. There is a clear trend of EC-carbon lattice interactions strengthening at sites away from the surface top. Interestingly, the EC interaction with the carbon lattice seems unaffected by the nature of the defect in most cases, where similar adsorption energies are shown for different defects. One clear difference is seen at P2 and P5, where EC shows stronger adsorption energy at O_C and V_C sites than on the $2O_C$ and O_CV_C sites. The EC molecule on the abrupt surface shows a similar trend (Figure 4 and Figure S7, Supporting Information), with only the O_C and $2O_C$ defects showing any significant interaction with the EC molecule, but at very low adsorption energies (–0.38 and –0.33 eV, respectively). For the O_CV_C and V_C defect, a clear repulsive interaction is seen (1.02 and 0.77 eV, respectively). For the defective basal plane surfaces, the EC is most strongly bonded to the $2O_C$ defect (E_{ads} = –1.39 eV), and shows similar adsorption energy for the other defects ($E_{ads,Oc}$ = –0.61 eV, $E_{ads,OcVc}$ = –0.54 eV, and $E_{ads,Vc}$ = –0.52 eV). Comparing these adsorption energies to those previously calculated for Na at the same defective basal planes,[10,24] it is clear that Na adsorption is more energetically favorable than EC adsorption, apart from the $2O_C$ defect. Therefore, one can speculate that no competition between Na and EC would be expected due to the much stronger affinity for Na storage at these defect sites. In the case of $2O_C$, the higher EC binding energy would lead to the potential blocking of Na adsorption sites, proportional to the $2O_C$ defect concentration.

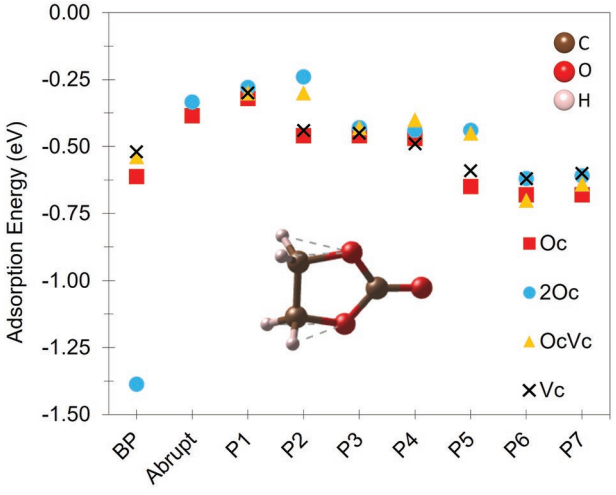

Figure 4. EC (with molecular inset figure of EC molecule where brown spheres are carbon, red oxygen, and white hydrogen) adsorption energy at the defect sites in the basal plane (BP), abrupt, and defect positions P1–P7 corresponding to those in Figure 1b. The optimized structures of these are included in Figures S5–S7, Supporting Information.

2.3. Adsorption of the EC Breakdown Products at Defect Sites

Breakdown mechanisms of EC have been investigated in previous computational work,[34–36] which identified the lowest energy pathway as the dissociative EC → CO_3^{2-} + C_2H_4 (for convenience CO_3^{2-} will henceforth be referred to as CO_3).[34] At the surface, the EC shows the most favorable binding at the $2O_c$ defect at the basal plane (Figure 4), although does not lead to breakdown (Figure S6d, Supporting Information). In the absence of a clearly identified EC breakdown site involving the individual defects considered, it is reasonable to surmise that the binding followed by breakdown most likely occurs at extended O-defect clusters. To explore the stability and binding of the most favorable breakdown products (CO_3 and C_2H_4), the adsorption energy in the defective rough models (with each defect at different lattice positions P1–P7) is calculated (as shown in **Figure 5**, with optimized geometries shown in Figures S8 and S9, Supporting Information), in comparison to the adsorption energy on the basal plane and the curved surface with the same defects.

As shown in Figure 5a, the EC breakdown product C_2H_4 shows very weak interaction with most of the defects, aside from the positional variations of the defects in the rough model moving from surface adsorption to intercalation. For CO_3 on the basal plane, the magnitude of the binding at the $2O_C$ site is similar to that of Na adsorption (–0.67 eV),[24] resulting in competition between Na and the fragments thereby reducing the effective Na capacity.

The CO_3 fragment proves to be more reactive, showing much stronger adsorption energies (Figure 5b) when compared to those of EC and C_2H_4 (Figures 4 and 5a). This stronger interaction was observed to lead to the breakdown of CO_3 to CO_2 and an oxygen functional group at the defect site (a variety of breakdown sites and positions are possible as shown in Figure S9, Supporting Information), functionalizing the surface. Figure 5b shows the variation in adsorption energy, where on the P1 site (surface top) O_C shows the same behavior as described for the abrupt surface (Figure S7o, Supporting Information), with C=O added to the unsaturated C, opposite the two-fold O (**Figure 6**a). This oxygen functional group is similar to the C=O

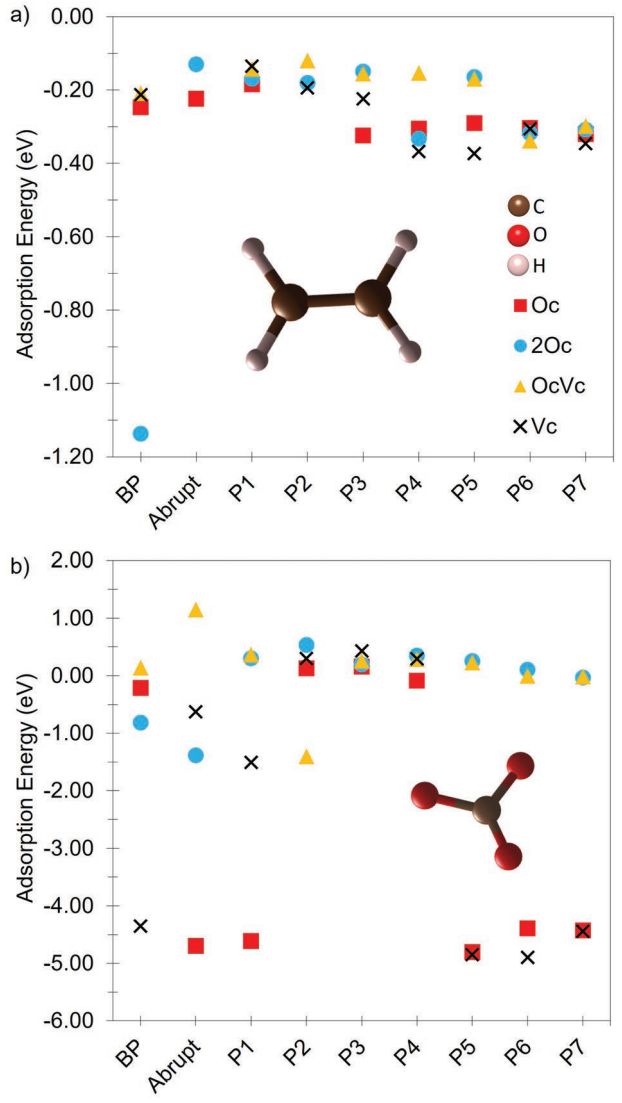

Figure 5. EC fragment a) C_2H_4 and b) CO_3 adsorption energies on defect sites in the basal plane (BP), abrupt, and rough (at different positions P1–P7 according to Figure 1b) models. Insets show molecular fragments in each case where brown spheres are carbon, red oxygen, and white hydrogen.

motif identified to be energetically favorable at the abrupt surface in our previous work,[11] indicating that this might be one of the origins of these functional groups in HC anodes. V_C by contrast shows an intermediate behavior, with the CO_3 bound to the V_C via the unsaturated C and the O—CO_2 (Figure 6b). As can be seen from Figure 6b, this leads to distortion in the intramolecular C—O bonds in the CO_3 fragment, with elongation of the C—O bonds at the O bonded to the surface carbon of 0.1 Å, and a contraction of the C—O bond that is oriented away from the surface of 0.07 Å. The C—O bonds to the carbon surface are noticeably longer than the carbon-oxygen bond lengths obtained for Figure 6a, which is also reflected in the weaker adsorption energy of CO_3 at V_C site P1 as compared to O_C site P1 (Figure 6b). In the intercalation regime, both the O_C and V_C show the addition of C=O to the unsaturated lattice C in positions P5–P7, coupled with the liberation of CO_2 (Figure 6c,d (showing the position of the CO_2 within the trough region), and Figure S9, Supporting Information). CO_2 liberation was also observed for CO_3 at V_C on the basal plane (see Figure S6, Supporting Information), where the optimized structure showed a C=O added to the unsaturated vacancy-C and CO_2 moving away from the surface (>4 Å). A schematic representation of the different mechanisms is provided in Figure 6e. O_C and O_CV_C adsorption are significantly less favored with O_CV_C showing a repulsive interaction. Whilst the $2O_C$ shows enhanced adsorption, the CO_3 remains intact although moving toward the C-surface. For the same defect and fragment on the abrupt surface, however, in the absence of a perpendicular C-dangling bond, the O is added to an adjacent C, initially as C=O, which can then undergo relaxation to give the C—O—C. Hence, the O-functionalization is added to both planar, and curved surfaces as previously described.[11]

2.4. AIMD Investigation of EC Binding and Breakdown

From the above discussion, it is clear that some sites can bind EC and C_2H_4 ($2O_C$ on the BP), and CO_3. The breakdown of CO_3 and the liberation of CO_2 is spontaneous in systems with a number of unsaturated C-bonds, provided either by the vacancy or O_C defects. A disordered surface model is prepared to provide a high concentration of dangling bonds; for simplicity, only C-dangling bonds are considered. **Figure 7**a shows the initial disordered interface and the same system after 25 ps at 330 K (Figure 7b). Some features of interest are immediately evident: H-abstraction (Figure 7c), O-loss (Figure 7d), surface EC binding (Figure 7e), and EC dissociation (Figure 7f). These configurations shown in Figure 7c–f point to the initial binding and breakdown modes of EC when presented with a high concentration of surface dangling bonds (unsaturated C-atoms). It is worth mentioning that the role of roughness and further breakdown of the identified fragments is the subject of the ongoing investigation.

2.5. Experimental Characterization

From the above analysis, it is clear that in the majority of cases, these carbon surfaces would not trap EC or its fragments, but oxygen functionalization and occupation of possible Na sites are expected at the O_C and V_C defect sites. To validate these results, we studied experimentally two HC materials[6] with different microstructures that were discharged in an EC-based electrolyte, ST1000 and ST1500. ST1000 consists of graphitic pores with larger average spacing between the graphitic planes (3.76 Å from small-angle X-ray scattering (SAXS)/wide-angle X-ray scattering (WAXS) measurements for ST1000 and 3.68 Å for ST1500), has a larger concentration of defects, and smaller average micropore diameter (1.75 nm for ST1000 and 2.2 nm for ST1500) than the ST1500 HC material. ST1500 furthermore has a more graphitic structure with larger basal plane (which are graphene-like) domains and a larger graphitic layer stack thickness than ST1000.[6] To obtain information on the depth profile of the SEI composition, X-ray photoelectron spectroscopy

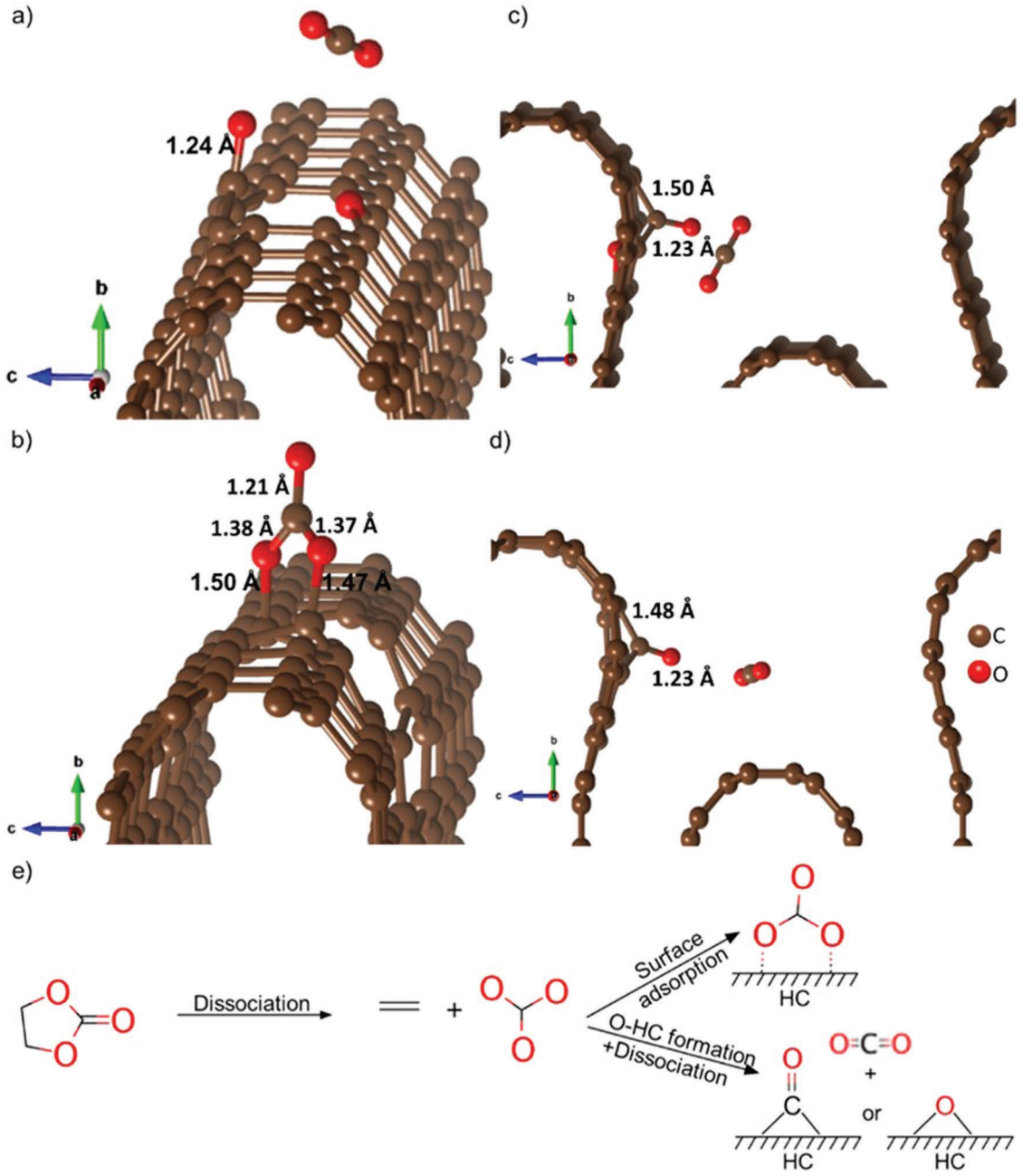

Figure 6. Optimized structures of CO_3 (and its breakdown products) with annotated bond lengths on the a) O_C defect at position P1, b) V_C defect at position (for reference the C—O bond lengths in the free CO_3 unit is 1.28 Å), c) at O_C defect at position P6, and d) at V_C defect at position P6, with e) a schematic representation of the different mechanisms. Brown spheres are carbon atoms, and red oxygen. The C=O bond distance in the CO_2 molecules is 1.18 Å.

(XPS) spectra (**Figure 8**) were acquired for the unsputtered sodiated samples, and then after sequential removal (30 s intervals) of thin surface layers, to generate a composition depth profile shown in Figure S11 and Tables S1 and S2, Supporting Information.

After sodiation of the electrodes ($x = 0$), the sp^2 carbon peak in the C 1s spectra (Figure S11, Supporting Information) arising from the graphitic features of HC almost disappeared for both electrodes. This is an indication of a layer covering the surface of the HC, which could be linked to the decoration of HC surfaces at defect sites as observed from the computational results. As the etching time increases, the concentration of C=O decreases more rapidly in the ST1500 material (Figure 8). The ST1000 material is more defective than the ST1500[6] (Figure 8). As seen from the C1s peak contributions (Figure S11 and Tables S1 and S2, Supporting Information), ST1000 has a higher degree of C—O and C=O-containing organic compound on the surface, therefore, it is expected to have a thicker SEI layer,

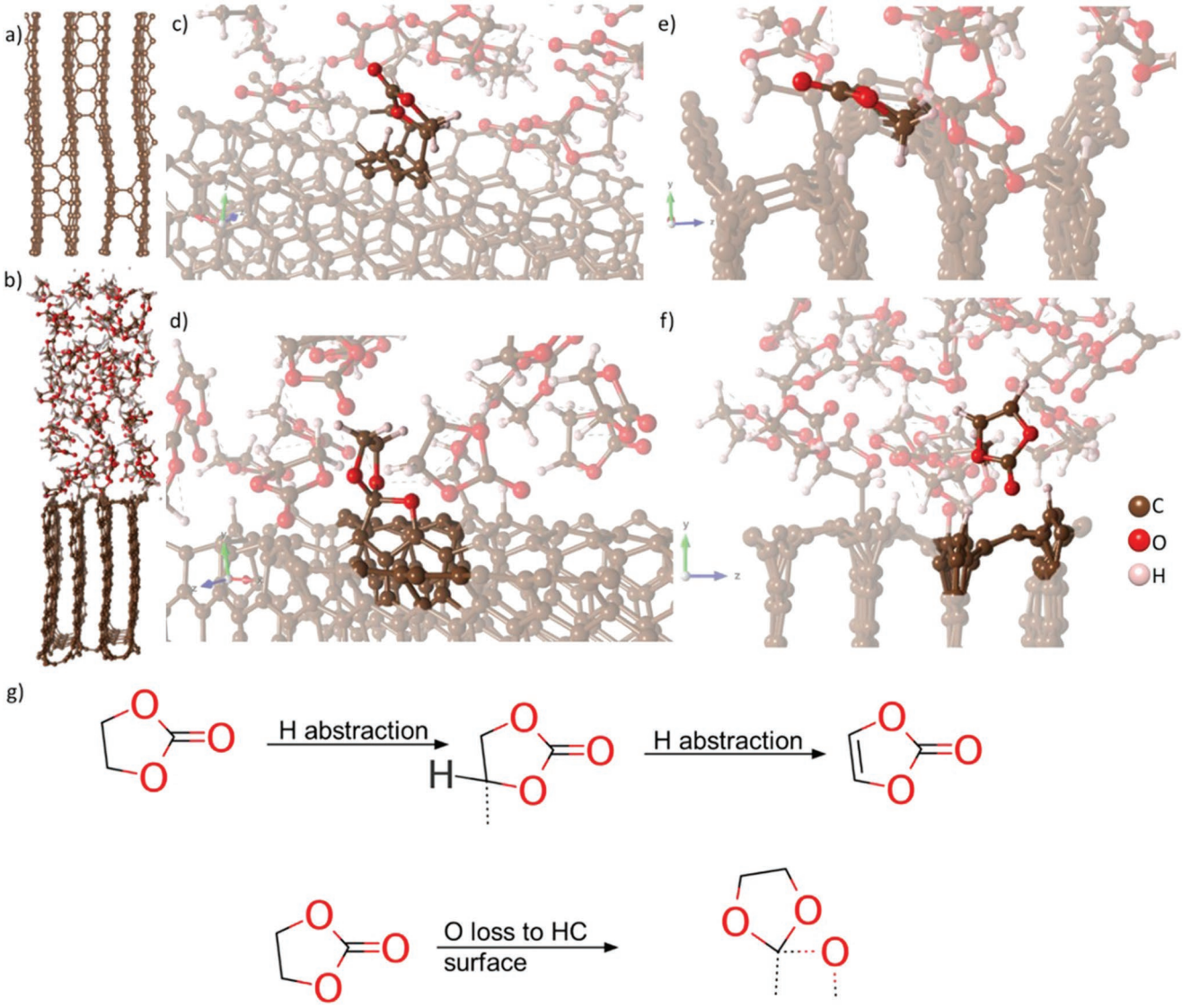

Figure 7. a) Disordered carbon surface (top view) used for disordered carbon surface EC AIMD simulations, and b) the full cell after 25 ps AIMD simulation. c) Hydrogen abstraction from an EC molecule at 3.82 ps after equilibration, d) oxygen loss from EC to carbon surface at 6.84 ps after equilibration, e) EC interaction with surface at 25 ps after equilibration, and f) formation of vinylene carbonate through H loss to the disordered surface at 13.54 ps after equilibration. A schematic view of the different observed EC breakdown mechanisms is shown in (g), with a zoomed-in view of (c–f) provided in Figure S10, Supporting Information.

confirming the simulation results presented here and also previously.[6,8,10,11,23,24] It should be also considered that argon and oxygen form a strong donor–acceptor chemical bond, therefore, Ar^+ sputtering might be causing the reduction of C—O bonds and change the surface chemistry. Combining the computational and experimental insights into the EC-carbon surface interaction, it could be shown that the presence of defects and curved motifs influence electrolyte breakdown and immobilization. Coupling these results to those of the sodiation of HC anodes, a series of materials considerations for the design of HC anodes could be made. HC materials, as stated in Section 1, are complex materials with a tunable structure, making them excellent for targeted materials design. The main structural motifs of HCs are graphene basal planes, graphitic pores with variable interlayer distance, and curved nanopores and surfaces. The results presented in this work show that the shape of the carbon motifs (basal plane vs rough surface) has a direct impact not only on the sodiation[6,9–12,23,24,42,43] but also on the EC interaction. In general, the basal planes have higher defect formation energy than the curved motifs, indicating that the defect concentration under equilibrium conditions in the basal plane motifs would be lower.[10,23,24] Oxygen defects and the formation of C—O and C=O bonds were shown to lead to thicker SEIs and have previously been shown to give a significant contribution to the NIB *I–V* curve sloping regions.[10] As noted previously for the sodiation of HC materials, oxygen heteroatoms are beneficial for the initial sodium storage but could contribute to irreversible capacity if present in significant concentrations due

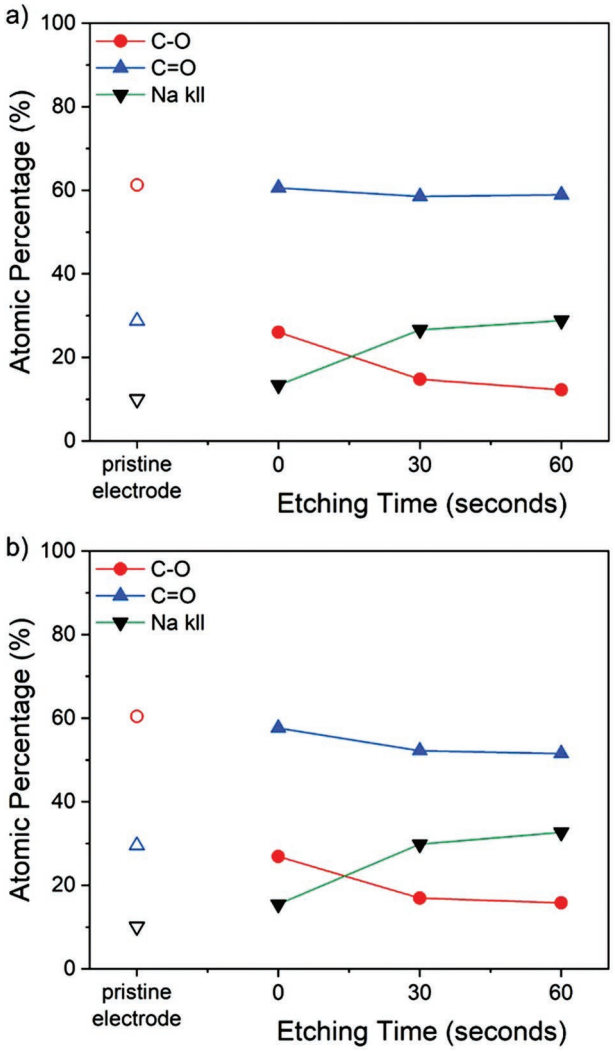

Figure 8. The atomic fractions calculated from the O1s spectra of a) ST1000 and b) ST1500 HC anode (pristine electrode), cycled in 1 M $NaPF_6$ in EC ($x = 0$), after 30 s of etching ($x = 30$), and after 60 s of etching ($x = 60$).

to their strong Na adsorption energies.[10,11,23,24,43,44] The effect of these defects on EC adsorption is not as pronounced. Their interaction with the breakdown fragments of carbonates (especially CO_3) can be significant as observed in Figure 5, which could lead to an increase in oxygen functional groups and CO_2 outgassing.[11,45] This could also explain why HC with a higher C—O and C=O concentration have thicker SEIs and should be considered when designing future HC anode materials. It is also clear from the work here that any undercoordinated HC site (i.e., that leads to an unsaturated carbon site) is a possible EC breakdown site, leading to increased defect concentration and the possibility of crosslinking (which has previously been observed for carbon vacancies in similar systems).[23] Future studies will also show how other electrolyte molecules interact with these HC motifs, adding further materials design considerations. The challenge remains in linking the computationally optimized HC material to a synthetic route.

3. Conclusions

In this paper, we have performed a series of DFT and AIMD simulations together with XPS experiments to probe the effect of anode surface roughness and defects on HC-EC interactions at the electrolyte–anode interface in NIBs. We have proposed a new rough model for HC and compared it with the commonly used basal plane and abrupt models. Practical NIBs are more complex than the model presented in this paper, and future studies could also take into account the effect of Na (and also other cations as HC is employed as an anode material in a variety of battery technologies), other electrolyte solvents and the counter anion of the electrolyte salt. The interaction of other carbonate solvents with similar breakdown products to EC would be expected to act similarly, but the longer carbon chains and different chemistries of non-carbonate electrolyte solvents may lead to different HC interactions. It would further also be instructive to elucidate the effect of binder on the electrolyte–anode interface and the overall battery performance.

DFT studies showed that for HC surface without defects, EC only interacts weakly with the carbon surface, and does not limit Na storage capacity by occupying Na storage sites. EC would only be expected to impact the Na storage capacity and compete with Na for carbon surface storage sites at $2O_C$ defects. Probing the adsorption of EC fragments C_2H_4 and CO_3 on the HC model, it was shown that CO_3 has the strongest interaction with the HC surface. For sites with carbon-dangling bonds, a breakdown of the CO_3 was observed. This breakdown leads to the formation of a CO_2 molecule and functionalization of the surface with CO groups, which could lead to increased oxygen concentration at HC anodes during cycling. From XPS analysis of the EC–HC interface in a cycled NIB cell, the computational findings were further verified with the more defective and oxygen-containing HC material (ST1000) having thicker SEI layers than the HC material (ST1500) with a lower heteroatom concentration.

4. Experimental Section

Computational Details: All DFT and AIMD simulations in this were carried out using the CP2K code.[46–49] Based on previous studies of metal–ion interactions with different carbon models, the PBE functional[50,51] and DFT-D3 method with Becke–Johnson damping[52–56] for the dispersion correction were selected.[11,12,23,24] All calculations were performed at the Γ-point with a plane wave cut-off of 650 Ry and the TZVP-SR-MOLOPT[47,57] basis set. All parameters were converged to 0.01 meV with respect to energy and 0.001 eV $Å^{-1}$ with respect to forces. The HC models contained 800 carbon atoms. For all HC models, bulk cell optimizations were first performed using a quasi-Newton algorithm with BFGS Hessian updating scheme[48,58,59,60–63] to fully relax the structure in terms of lattice parameters and ion positions, whereby the lattice parameters were kept fixed in the geometry optimizations for the defect studies. After the cell optimizations of the HC models, the lattice vectors were kept fixed for geometry optimizations (also performed using BFGS) of the defect systems and the molecule adsorption. The defects were considered in the dilute limit, with a single defect of each type per 800 atom HC surface model. This choice was to allow the individual defect–molecule (fragment) interaction to be understood in the absence of any defect–defect interaction. To study the interaction between EC (and its fragments) with the pristine and defective HC systems, the initial position of the molecule based upon the most favored basal plane

geometry was used. The whole system was then allowed to relax in a geometry relaxation. Other initial molecule geometries were tested, with the same final geometry obtained.

To investigate the interaction of EC molecules with the different carbon surfaces, DFT geometry optimizations of a single EC molecule at the different carbon surfaces were then performed to calculate the adsorption energy (E_{ads}).[64,65]

$$E_{ads} = E_{EC@carbon\ surface} - E_{EC} - E_{carbon\ surface} \quad (1)$$

Here, $E_{EC@carbon\ surface}$ is the total energy of EC adsorbed on the rough models, $E_{carbon\ surface}$ is the total energy of the rough models presented in Section 2.1, and E_{EC} is the total energy of an isolated EC molecule in vacuum. Using this convention, a negative E_{ads} indicated that the EC adsorption process was exothermic, and hence, energetically favorable. A positive E_{ads} on the other hand would indicate that the process was endothermic, and hence, energetically unfavorable. The defect formation energy was calculated according to Equation (2).[66]

$$E_f^{defect} = E_{defective} + \sum n_i \mu_i - E_{bulk} \quad (2)$$

In Equation (2), E_f^{defect} is the defect formation energy, $E_{defective}$ is the total energy of the defective carbon model, E_{bulk} is the total energy of the pristine carbon model, n_i is the number of species either added or removed in relation to the pristine model (i.e., oxygen or carbon), and μ_i is the chemical potential of oxygen and carbon, respectively, dependent on defect.

The AIMD simulations were conducted on the optimized carbon surfaces whilst in contact with the liquid phase EC (density = 1.32 g cm^{-3})[35,67] using an NVT ensemble at 300 K with a time step of 0.5 fs and a Nosé–Hoover thermostat.[68] The interphase models were equilibrated for 10 ps, whereafter a production run of 10 ps was conducted.

Experimental Details: HC materials were synthesized by a "soft templating technique" at 200 °C, under self-generated pressure, and using absolute ethanol as the solvent. Phloroglucinol (1,3,5-benzentriol, $C_6H_6O_3$) was used as a carbon precursor, and the triblock copolymer Pluronic F127 (poly(ethylene oxide)-block–poly(propylene oxide)-block–poly(ethylene oxide, PEO106PPO70-PEO106) was used as the template. The bi-functional (aldehyde and carboxylic acid groups) glyoxylic acid was employed to cross-link phloroglucinol. All chemicals were purchased from Sigma-Aldrich and used as received. In a typical experiment, 0.82 g phloroglucinol and 0.61 g glyoxylic acid monohydrate were mixed with 1.61 g Pluronic F127 and dissolved under stirring at room temperature in 40 mL absolute ethanol. The obtained clear solution was transferred into 100 mL Teflon inlets, which were placed in stainless steel autoclaves (Parr Instruments). The mixture was heated up to 80 °C for 4 h to form the phenolic resin framework and the solvothermal treatment was subsequently done at 200 °C for 12 h. The materials were then filtered, dried at 80 °C and further pyrolyzed at 1000 °C (ST1000) and 1500 °C (ST1500) with a heating rate of 5 °C min^{-1} and a dwell time of 2 h under inert N_2 atmosphere.

Electrodes were made using an 85:5:10 weight ratio of active material, carbon black (Super P conductive, 99+%, Alfa Aesar), and carboxymethyl cellulose (CMC) binder (Mw ≈ 250000, Sigma Aldrich) in water. The obtained slurry was coated in a 250 µm layer on Al foil (conductive carbon coated, 18 µm, MTI corporation) by a doctor blade and dried at room temperature for 24 h and then at 100 °C for 2 h under vacuum. The foils were cut to a given diameter (usually 13 mm diameter) with a punch cutter. The electrolyte and half-cell preparation were conducted in an argon-filled glove box with H_2O < 0.5 ppm, and O_2 < 0.5 ppm. The CR2032 coin cells were assembled with a sodium metal disc (1 mm thick, sodium ingot, 99.8% metals basis, Alfa Aesar) as a counter electrode (CE), and an HC anode as the working electrode (WE). The loading of electrode active materials on the current collector ranged from 2.5–5 mg cm^{-2}. Whatman GF/B glass microfiber was used as a separator. A 1 M electrolyte solution containing predried (80 °C overnight) sodium hexafluorophosphate ($NaPF_6$ Alfa Aesar, 99+%) in melted EC (EC, anhydrous 99%, Sigma Aldrich), was prepared by stirring until fully dissolved. Galvanostatic cycling tests were performed on a Land system in the potential range of 0.001–2.5 V versus Na^+/Na for half-cell configuration. The discharge current rate was 30 mA g^{-1} which corresponds to a cycling rate of C/10.

XPS measurements were recorded on a system equipped with an Al (Kα) source operating at 2×10^{-9} mbar base pressure at ambient temperature. The spot size was 400 μm^2, and a flood gun was operating during acquisition. Atomic compositions of the pristine electrodes were obtained from the averaged spectra taken from three areas for each sample (13 mm diameter). For ex situ sputtering measurements (taken from three areas for each sample), after the coin cell disassembly, the recovered electrodes were carefully washed several times with melted EC. Then the washed electrodes were dried for 6 h to fully evaporate the solvent and then transferred to the vacuum transfer container. Argon sputtering for the XPS depth-profiling was carried out using ion beam energies of 500 eV. The etching rate calibrated on the Tantalum pentoxide (Ta_2O_5) surface was ≈0.05 nm s^{-1}. The quantitative analyses were performed using Casa XPS software. The binding energies were corrected to the C 1s peak position at 284.8 eV originating from surface hydrocarbons.

Statistical Analysis: The binding energies were corrected to the C 1s peak position at 284.8 eV originating from surface hydrocarbons. Shirley background function was applied and subtracted from the data. The peaks were fitted using a convolution of Gaussian and Lorentzian peak shapes. C1s and O 1s spectra were analyzed. The binding energies were corrected to the C 1s peak position at 284.8 eV originating from surface hydrocarbons. Mean values for atomic percentage are presented in Figure 8 and Figure S11, Supporting Information, with mean ± SD given in Tables S1 and S2, Supporting Information.

Supporting Information

Supporting Information is available from the Wiley Online Library or from the author.

Acknowledgements

The authors would like to thank the Engineering and Physical Sciences Research Council for funding (Grant No. EP/R021554/2). E.O. would like to thank the University of Surrey for access to its High-Performance Computing facility and the Eureka HPC cluster, and funding from the University of Surrey Academic Disruption Fund. Via membership of the UK's HEC Materials Chemistry Consortium, which was funded by EPSRC (EP/L000202), this work used the UK Materials and Molecular Modelling Hub for computational resources, MMM Hub, which was partially funded by EPSRC (EP/P020194 and EP/T022213). H.Au. would like to thank the Faraday Institution's LiSTAR project (EP/S003053/1, Grant FIRG014) for funding. M.C.-R. acknowledges the EPSRC grant EP/S018204/2 (UK-China Low Carbon Manufacturing call). Part of this work has been carried out within ARCNL, and made use of the Dutch national e-infrastructure with the support of the SURF Cooperative using grant no. EINF-2434. The authors thank SURF (www.surf.nl) for the support in using the Lisa Compute Cluster and National Supercomputer Snellius. E.O. is grateful for a WISE Fellowship from the Dutch Research Council (NWO).

Conflict of Interest

The authors declare no conflict of interest.

Data Availability Statement

The data that support the findings of this study are available from the corresponding author upon reasonable request.

Keywords

anodes, batteries, density functional theory, ethylene carbonate, hard carbon, sodium, X-ray photoelectron spectroscopy

Received: January 10, 2022
Revised: July 29, 2022
Published online:

[1] P. K. Nayak, L. Yang, W. Brehm, P. Adelhelm, *Angew. Chem., Int. Ed.* **2018**, *57*, 102.
[2] J. B. Goodenough, *Energy Environ. Sci.* **2014**, *7*, 14.
[3] P. Thomas, D. Billaud, *Electrochim. Acta* **2001**, *46*, 3359.
[4] C. Bommier, D. Mitlin, X. Ji, *Prog. Mater. Sci.* **2018**, *97*, 170.
[5] W. Luo, F. Shen, C. Bommier, H. Zhu, X. Ji, L. Hu, *Acc. Chem. Res.* **2016**, *49*, 231.
[6] H. Alptekin, H. Au, E. Olsson, J. Cottom, A. Jensen, T. Headen, A. Drew, Q. Cai, M. Titirici, M. Ribadeneyra, *Adv. Mater. Interfaces* **2021**, *9*, 2101267.
[7] Y. Li, Y. Lu, P. Adelhelm, M.-M. Titirici, Y.-S. Hu, *Chem. Soc. Rev.* **2019**, *48*, 4655.
[8] H. Au, H. Alptekin, A. C. S. Jensen, E. Olsson, C. A. O'Keefe, T. Smith, M. Crespo-Ribadeneyra, T. F. Headen, C. P. Grey, Q. Cai, A. J. Drew, M.-M. Titirici, *Energy Environ. Sci.* **2020**, *13*, 3469.
[9] A. C. S. Jensen, E. Olsson, H. Au, H. Alptekin, Z. Yang, S. Cottrell, K. Yokoyama, Q. Cai, M.-M. Titirici, A. J. Drew, *J. Mater. Chem. A* **2020**, *8*, 743.
[10] H. Alptekin, H. Au, A. C. S. Jensen, E. Olsson, M. Goktas, T. F. Headen, P. Adelhelm, Q. Cai, A. J. Drew, M.-M. Titirici, *ACS Appl. Energy Mater.* **2020**, *3*, 9918.
[11] E. Olsson, J. Cottom, H. Au, M.-M. M. Titirici, Q. Cai, *Carbon* **2021**, *177*, 226.
[12] E. Olsson, J. Cottom, H. Au, Z. Guo, A. C. S. Jensen, H. Alptekin, A. J. Drew, M.-M. Titirici, Q. Cai, *Adv. Funct. Mater.* **2020**, *30*, 1908209.
[13] M. M. Titirici, R. J. White, C. Falco, M. Sevilla, *Energy Environ. Sci.* **2012**, *5*, 6796.
[14] Y. Li, Y.-S. S. Hu, M.-M. M. Titirici, L. Chen, X. Huang, *Adv. Energy Mater.* **2016**, *6*, 1600659.
[15] J. Deng, W.-B. Luo, S. L. Chou, H. K. Liu, S. X. Dou, *Adv. Energy Mater.* **2018**, *8*, 1701428.
[16] J. Conder, C. Vaulot, C. Marino, C. Villevieille, C. M. Ghimbeu, *ACS Appl. Energy Mater.* **2019**, *2*, 4841.
[17] M. Dahbi, M. Kiso, K. Kubota, T. Horiba, T. Chafik, K. Hida, T. Matsuyama, S. Komaba, *J. Mater. Chem. A* **2017**, *5*, 9917.
[18] X. Dou, I. Hasa, D. Saurel, C. Vaalma, L. Wu, D. Buchholz, D. Bresser, S. Komaba, S. Passerini, *Mater. Today* **2019**, *23*, 87.
[19] Q. Meng, Y. Lu, F. Ding, Q. Zhang, L. Chen, Y. S. Hu, *ACS Energy Lett.* **2019**, *4*, 2608.
[20] C. Chen, M. Wu, Y. Wang, K. Zaghib, *J. Power Sources* **2019**, *444*, 227310.
[21] J. M. Stratford, P. K. Allan, O. Pecher, P. A. Chater, C. P. Grey, *Chem. Commun.* **2016**, *52*, 12430.
[22] F. Xie, Z. Xu, Z. Guo, M.-M. Titirici, *Prog. Energy* **2020**, *2*, 042002.
[23] E. Olsson, J. Cottom, Q. Cai, *Small* **2021**, *17*, 2007652.
[24] E. Olsson, G. Chai, M. Dove, Q. Cai, *Nanoscale* **2019**, *11*, 5274.
[25] G. G. Eshetu, T. Diemant, M. Hekmatfar, S. Grugeon, R. J. Behm, S. Laruelle, M. Armand, S. Passerini, *Nano Energy* **2019**, *55*, 327.
[26] F. A. Soto, P. Yan, M. H. Engelhard, A. Marzouk, C. Wang, G. Xu, Z. Chen, K. Amine, J. Liu, V. L. Sprenkle, F. El-Mellouhi, P. B. Balbuena, X. Li, *Adv. Mater.* **2017**, *29*, 1606860.
[27] R. Mogensen, D. Brandell, R. Younesi, *ACS Energy Lett.* **2016**, *1*, 1173.
[28] S. J. An, J. Li, C. Daniel, D. Mohanty, S. Nagpure, D. L. Wood, *Carbon* **2016**, *105*, 52.
[29] R. Jorn, R. Kumar, *Electrochem. Soc. Interface* **2017**, *26*, 55.
[30] L. F. Zhao, Z. Hu, W. H. Lai, Y. Tao, J. Peng, Z. C. Miao, Y. X. Wang, S. L. Chou, H. K. Liu, S. X. Dou, *Adv. Energy Mater.* **2021**, *11*, 2002704.
[31] O. Borodin, X. Ren, J. Vatamanu, A. von Wald Cresce, J. Knap, K. Xu, *Acc. Chem. Res.* **2017**, *50*, 2886.
[32] E. Irisarri, A. Ponrouch, M. R. Palacin, *J. Electrochem. Soc.* **2015**, *162*, A2476.
[33] A. Ponrouch, M. R. Palacín, *Electrochem. Commun.* **2015**, *54*, 51.
[34] P. Watthaisong, S. Suthirakun, P. Hirunsit, *J. Phys. Chem. C* **2021**, *125*, 8031.
[35] J. M. M. De La Hoz, K. Leung, P. B. Balbuena, *ACS Appl. Mater. Interfaces* **2013**, *5*, 13457.
[36] J. Young, M. Smeu, *J. Phys. Chem. Lett.* **2018**, *9*, 3295.
[37] J. Yu, P. B. Balbuena, J. Budzien, K. Leung, *J. Electrochem. Soc.* **2011**, *158*, A400.
[38] K. Wang, Y. Xu, Y. Li, V. Dravid, J. Wu, Y. Huang, *J. Mater. Chem. A* **2019**, *7*, 3327.
[39] A. Beda, C. Villevieille, P.-L. Taberna, P. Simon, C. M. Ghimbeu, *J. Mater. Chem. A* **2020**, *8*, 5558.
[40] K. Kubota, S. Shimadzu, N. Yabuuchi, S. Tominaka, S. Shiraishi, M. Abreu-Sepulveda, A. Manivannan, K. Gotoh, M. Fukunishi, M. Dahbi, S. Komaba, *Chem. Mater.* **2020**, *32*, 2961.
[41] V. G. Pol, J. Wen, K. C. Lau, S. Callear, D. T. Bowron, C. K. Lin, S. A. Deshmukh, S. Sankaranarayanan, L. A. Curtiss, W. I. F. David, D. J. Miller, M. M. Thackeray, *Carbon* **2014**, *68*, 104.
[42] E. Olsson, T. Hussain, A. Karton, Q. Cai, *Carbon* **2020**, *163*, 276.
[43] H. Au, H. Alptekin, A. Jensen, E. Olsson, C. A. O'Keefe, T. Smith, M. Crespo-Ribadeneyra, T. Headen, C. P. Grey, Q. Cai, A. Drew, M. Titirici, *Energy Environ. Sci.* **2020**, *13*, 3469.
[44] E. Olsson, J. Yu, H. Zhang, H. Cheng, Q. Cai, *Adv. Energy Mater.* **2022**, *12*, 2200662.
[45] C. M. Ghimbeu, J. Górka, V. Simone, L. Simonin, S. Martinet, C. Vix-Guterl, *Nano Energy* **2018**, *44*, 327.
[46] J. Vandevondele, M. Krack, F. Mohamed, M. Parrinello, T. Chassaing, J. Hutter, *Comput. Phys. Commun.* **2005**, *167*, 103.
[47] J. Vandevondele, J. Hutter, *J. Chem. Phys.* **2007**, *127*, 114105.
[48] J. Hutter, M. Iannuzzi, F. Schiffmann, J. Vandevondele, *Wiley Interdiscip. Rev. Comput. Mol. Sci.* **2014**, *4*, 15.
[49] K. Burke, F. G. Cruz, K.-C. Lam, *J. Chem. Phys.* **1998**, *109*, 8161.
[50] J. Perdew, K. Burke, M. Ernzerhof, *Phys. Rev. Lett.* **1997**, *77*, 3865.
[51] J. Perdew, K. Burke, M. Ernzerhof, *Phys. Rev. Lett.* **1997**, *77*, 1396.
[52] A. D. Becke, E. R. Johnson, *J. Chem. Phys.* **2005**, *123*, 154101.
[53] E. R. Johnson, A. D. Becke, *J. Chem. Phys.* **2006**, *124*, 174104.
[54] S. Grimme, S. Ehrlich, L. Goerigk, *J. Comput. Chem.* **2011**, *32*, 1456.
[55] S. Grimme, J. Antony, S. Ehrlich, H. Krieg, *J. Chem. Phys.* **2010**, *132*, 154104.
[56] S. Grimme, J. Antony, T. Schwabe, C. Mück-Lichtenfeld, *Org. Biomol. Chem.* **2007**, *5*, 741.
[57] M. Guidon, J. Hutter, J. Vandevondele, *J. Chem. Theory Comput.* **2010**, *6*, 2348.
[58] T. D. Kühne, M. Iannuzzi, M. del Ben, V. V. Rybkin, P. Seewald, F. Stein, T. Laino, R. Z. Khaliullin, O. Schütt, F. Schiffmann, D. Golze, J. Wilhelm, S. Chulkov, M. H. Bani-Hashemian, V. Weber, U. Borštnik, M. Taillefumier, A. S. Jakobovits, A. Lazzaro, H. Pabst, T. Müller, R. Schade, M. Guidon, S. Andermatt, N. Holmberg, G. K. Schenter, A. Hehn, A. Bussy, F. Belleflamme, G. Tabacchi, et al., *J. Chem. Phys.* **2020**, *152*, 194103.
[59] J. D. Head, M. C. Zerner, *Chem. Phys. Lett.* **1985**, *122*, 264.
[60] C. G. Broyden, *IMA J. Appl. Math.* **1970**, *6*, 76.
[61] D. F. Shanno, *Math. Comput.* **1970**, *24*, 647.
[62] R. Fletcher, *Comput. J.* **1970**, *13*, 317.

[63] D. Goldfarb, *Math. Comput.* **1970**, *24*, 23.
[64] Z. Xu, X. Lv, J. Chen, L. Jiang, Y. Lai, J. Li, *Carbon* **2016**, *107*, 885.
[65] S. Yang, S. Li, S. Tang, W. Dong, W. Sun, D. Shen, M. Wang, *Theor. Chem. Acc.* **2016**, *135*, 164.
[66] S. Zhang, J. Northrup, *Phys. Rev. Lett.* **1991**, *67*, 2339.
[67] M. S. Khan, A. V. Karatrantos, T. Ohba, Q. Cai, *Phys. Chem. Chem. Phys.* **2019**, *21*, 22722.
[68] S. Nosé, *J. Chem. Phys.* **1984**, *81*, 511.

